Probing exchange bias at the surface of a doped ferrimagnetic insulator

Yang Wang,[1] Xiao Wang,[2] Andy T. Clark,[2] Hang Chen,[1] Xuemei M. Cheng,[2] John W. Freeland,[3] and John Q. Xiao[1,*]

[1]*Department of Physics and Astronomy, University of Delaware, Newark, Delaware 19716, USA*

[2]*Department of Physics, Bryn Mawr College, Bryn Mawr, Pennsylvania 19010, USA*

[3]*Advanced Photon Source, Argonne National Laboratory, Lemont, Illinois 60439, USA*

(Received 16 April 2021; accepted 23 June 2021; published 26 July 2021)

With the realization of stress-induced perpendicular magnetic anisotropy, efficient spin-orbit torque switching, and room temperature topological Hall effect, interest in rare earth iron garnets has been revived in recent years for their potential in spintronic applications. In this study, we investigate the magnetic properties of micrometer-thick Bi and Ga substituted thulium iron garnets (BiGa:TmIG) grown by the liquid-phase epitaxy method. Above the magnetization compensation (MC) temperature, anomalous triple hysteresis is observed in BiGa:TmIG/Pt heterostructures by anomalous Hall effect measurements. X-ray magnetic circular dichroism and energy dispersive spectroscopy measurements reveal its origin as an internal exchange bias (EB) effect arising from inhomogeneities localized at the surface of the film. Possibly depending on the difference in thickness and defect realization of the EB layer, two types of magnetization reversal mechanisms, namely, the Stoner-Wohlfarth type and the reversible domain-wall motion type, are observed. Our results show that rich meta-magnetic phases exist in garnets close to MC, which can be robustly tuned by chemical composition engineering and conveniently probed by electrical transport measurements.

DOI: 10.1103/PhysRevMaterials.5.074409

I. INTRODUCTION

In ferrimagnetic (FI) rare earth-transition metal (RE-TM) alloys and compounds, the magnetic moments of the REs (Gd, Tb, Tm, etc.) and the TMs (Fe, Co and Ni) are antiferromagnetically (AF) coupled to each other. By changing composition or temperature, the RE and TM moments can cancel each other, resulting in a vanishing net magnetization. At this so-called magnetization compensation (MC) point, FIs resemble AFs, which makes them attractive as units in magnetic memory or logic devices for their immunity to external fields and ultrafast magnetization dynamics [1]. In the past few years, enhanced spin-orbit field [2], fast domain-wall motion [3], and ultrafast magnetization switching [4] have been demonstrated in RE-TM alloys close to compensation. Compared with these alloys, FI rare earth iron garnets (ReIG) have much higher chemical stability and lower Gilbert damping. As a prototypical FI insulator with perpendicular magnetic anisotropy (PMA) [5], thulium iron garnet $Tm_3Fe_5O_{12}$ (TmIG) has been shown to exhibit efficient spin-orbit torque switching [6] and above room temperature topological Hall effect [7]. However, partly because stoichiometric TmIG does not compensate above 1.5 K [8,9], phenomena around compensation have not been well explored.

A more traditional application of antiferromagnets is working as the exchange bias (EB) pinning layer in hard disks and spin valves. The EB effect [10,11] typically refers to the shift of the hysteresis of a ferromagnet (FM) in an AF/FM heterostructure caused by the atomic exchange coupling at the interface between the FM and the *uncompensated* AF. Interestingly, depending on whether being hard or soft, and whether close to or away from MC, FI can replace the AF or/and FM layers and create novel EB effects. Indeed, EB-related effects have been reported in AF/FI [12], FI/FM [13–15], and FI/FI [16] systems with *compensated* FI spin structures at the interface. Moreover, owing to the tunability of magnetic properties through composition variation, an inhomogeneous FI can exhibit a self-EB effect, which shows up as anomalous triple hysteresis. Such internal EB phenomenon has been studied in thick GdCo [17,18] and thin DyCo [19,20] films. It remains as an interesting question whether and how similar internal EB effect can form in ReIGs.

In this work, MC is introduced into TmIG films via changing the Tm/Fe ratio through cation doping. With anomalous Hall effect (AHE) and soft x-ray magnetic circular dichroism (XMCD) techniques, we observe triple hysteresis in a 14.1 μm-thick BiGa:TmIG film and identify its origin as an internal EB effect due to sample inhomogeneity. Energy dispersive spectroscopy (EDS) and control etching experiments confirm that the EB layer being close to the surface has a thickness in the $\sim$100 nm range at 140 K. When the thickness of the EB layer becomes thinner, a crossover from irreversible to reversible magnetization switching processes is observed. The latter is explained by a qualitative domain-wall formation model. Our results demonstrate doped ReIGs as a versatile playground to study EB effects and magnetization switching processes.

II. EXPERIMENTAL METHODS

The Bi and Ga substituted $Tm_3Fe_5O_{12}$ films were grown on both sides of (111)-oriented GGG substrates by the liquid-

*jqx@udel.edu

phase epitaxy (LPE) method [21,22]. High-purity Bi_2O_3, Tm_2O_3, Ga_2O_3, and Fe_2O_3 were mixed and melted in a platinum crucible while slowly rotating the substrate in the melt with a growth temperature of 900 °C. Right after taking out from the flux, the substrate was rotated at high speeds to remove the residual flux adhered to the sample surface. The crystalline quality of the sample was examined by x-ray diffraction (XRD, Rigaku) with a copper K-α radiation source. In-plane (IP) and out-of-plane (OP) magnetization versus field loops were obtained with a vibrating sample magnetometer (VSM, Quantum Design) in standard and oven modes. Chemical composition of the films was checked by EDS from both the sample surface and the cross-section. For transport measurement, we sputter-deposited 10 or 5 nm Pt films on the BiGa:TmIG films and patterned them into 100 × 200 μm Hall bar devices with standard photolithography and ion milling methods. Ti/Cu/Au electrodes were later formed by magnetron sputtering. AHE measurements were conducted with OP field scans mainly in a home-built cryogenic transport measurement system with a 4.5 kOe electromagnet. Measurements with larger fields were performed in a physical property measurement system (Quantum Design). XMCD experiments were carried out at the 4-ID-C beamline in the Advanced Photon Source at Argonne National Laboratory. The x-ray beam was incident at 45° off the normal of the BiGa:TmIG sample surface and external field was applied normal to the sample surface. Soft x-ray Fe L_3 and Tm M_5 peaks were first identified by saturating the magnetization in the OP direction while scanning the x-ray energy, and then Fe and Tm sublattice hysteresis were obtained by sweeping the external field with x-ray energy fixed at the peak of the XMCD at the L_3 and M_5 edges. All measurements were performed in the total fluorescence yield mode which has a probing depth of ~50 nm [23]. To recover the spin transmission transparency of the BiGa:TmIG surface from ion milling, a 5 min Piranha solution (H_2SO_4:H_2O_2 = 3 : 1) treatment [24,25] was adopted for some of the films.

III. RESULTS AND DISCUSSION

A. Magnetization compensation

As depicted in Fig. 1(a), eight formula units constitute a cubic unit cell of $Tm_3Fe_5O_{12}$. The 24 Fe^{3+} (d) ions at tetrahedral sites are AF coupled with the 16 Fe^{3+} (a) ions at octahedral sites, and the moments of the 24 Tm^{3+} (c) ions at dodecahedral sites are also antiparallelly aligned with Fe^{3+} (d) ions, both by superexchange interaction through the O^{2-} ions [27]. Because of the small moment of Tm, the magnetization of pure TmIG remains Fe dominant and does not exhibit compensation above 1.5 K [8,9]. However, this can be overcome by changing the Tm/Fe atomic ratio through chemical doping. As shown in Fig. 1(c), the XRD measurements of the front and back sides of a 14.1-μm thick BiGa:TmIG sample give almost identical peak locations and intensities, suggesting very similar bulk properties of the films on both sides of the substrate. The IP and OP *MH* loops reveal clear PMA [Fig. 1(d)]. The original purpose of introducing Bi^{3+} ions, which enter dodecahedral sites, was to enhance magneto-optical response [28] as well as growth-induced PMA [29], but in this study we focus on the effect

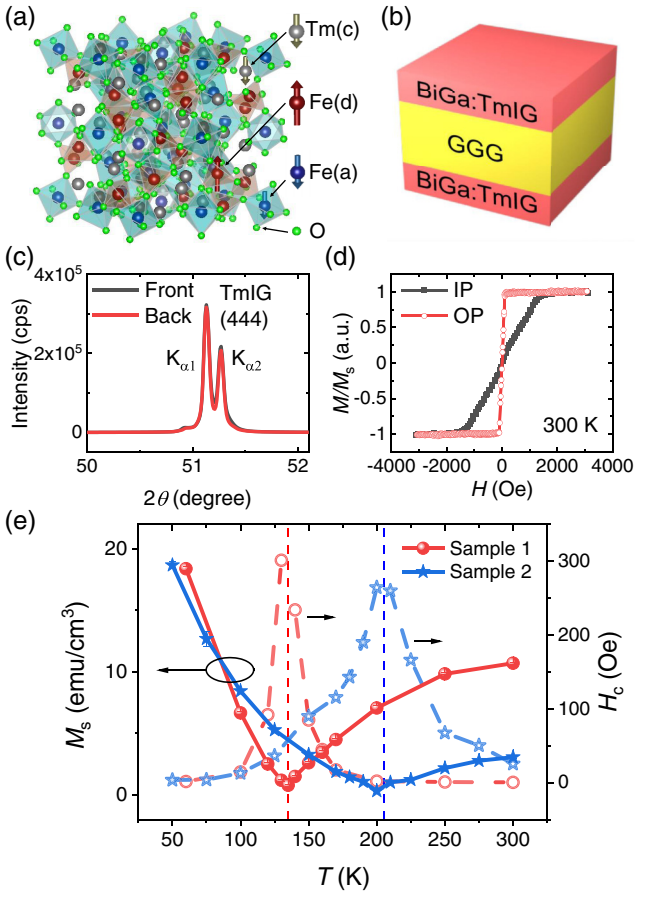

FIG. 1. (a) Illustration of a unit cell of Tm_3Fe_5O drawn with VESTA [26]. (b) Schematic of the structure of the LPE-grown BiGa:TmIG films. (c) XRD scans taken on both sides of the 14.1 μm thick BiGa:TmIG film. (d) *MH* loops measured by a VSM with IP and OP field scans. (e) Saturation magnetization (solid symbols) and coercivity (open symbols) as a function of temperature for Sample 1 ($Bi_{0.63}Tm_{2.36}Ga_{1.15}Fe_{3.85}O_{12}$, solid and open red circles) and Sample 2 ($Bi_{0.5}Tm_{2.5}Ga_{1.3}Fe_{3.7}O_{12}$, solid and open blue stars).

of Ga^{3+} ions which preferentially substitute Fe^{3+} (d) ions [27]. This causes a reduction in Fe sublattice magnetization and can give a compensation point for TmIG. As can be seen in Fig. 1(e), the disappearance of saturation magnetization together with the divergence of coercivity clearly show that MC is introduced in the above-measured sample with composition $Bi_{0.63}Tm_{2.36}Ga_{1.15}Fe_{3.85}O_{12}$ (Sample 1) as well as another 2-μm thick $Bi_{0.5}Tm_{2.5}Ga_{1.3}Fe_{3.7}O_{12}$ film (Sample 2) grown from a different melt. The chemical compositions were obtained by EDS from the surface of the films. Indeed, with a higher Tm/Fe ratio, the MC temperature, denoted as T_{MC} of Sample 2 (205 K), is higher than that of Sample 1 (135 K). In the following, the study is mainly focused on the front side of Sample 1 unless otherwise noted.

B. Anomalous hysteresis probed by AHE

As illustrated in Fig. 2(a), a charge current flowing in Pt injects spin currents into TmIG via the spin Hall effect (SHE) [30]. However, when the TmIG magnetization has a

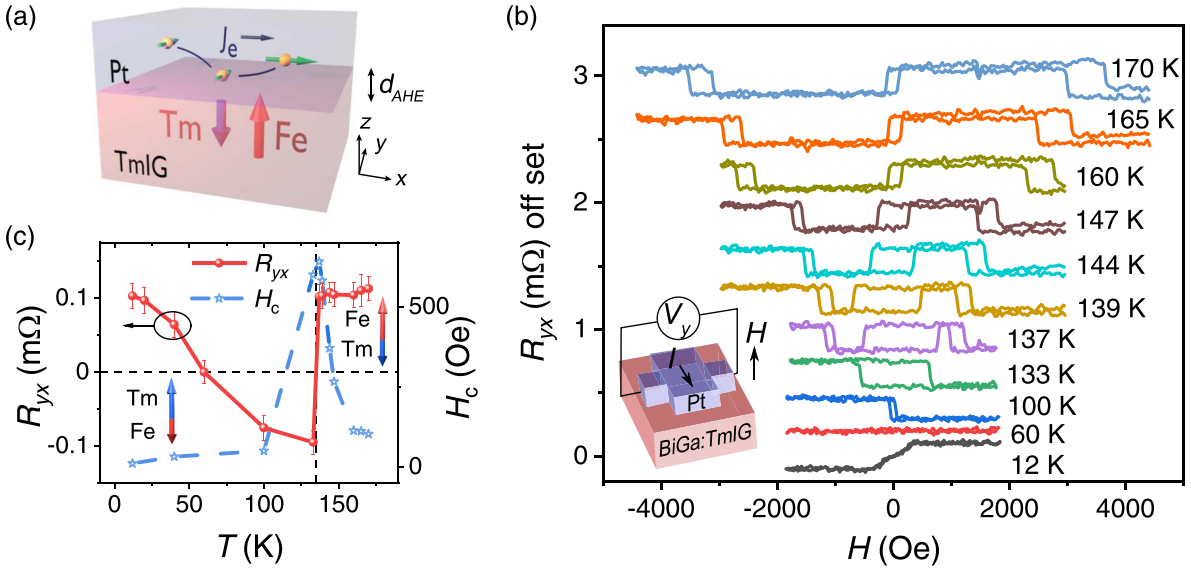

FIG. 2. (a) Schematic of the SH-AHE magnetometry. (b) AHE in the BiGa : TmIG(14.1 μm)/Pt(10 nm) Device 1. Field is applied in the OP direction and a linear background from the ordinary Hall effect is removed. (c) The temperature dependence of AHE resistance R_{yx} and coercivity H_c. Blue and red arrows represent the Tm and Fe sublattice magnetization, respectively.

finite z component, the imaginary part of the spin-mixing conductance causes a backflow of spin currents polarized in the longitudinal (x) direction. Consequently, these reflected spin currents generate an anomalous Hall voltage via the inverse SHE [31]. Since the spin currents mainly interact with the 3d transition metals [32], the sign and the magnitude of the Hall voltage solely reflect the orientation of the Fe sublattice magnetization. Because the dephasing length for transverse spins is only ∼1 nm in FMs [33] and less than 10 nm in nearly compensated FIs [32], the probing depth of this method is between 1 and 10 nm. Thus, this so-called SHE-induced AHE (SH-AHE) can be utilized as a local, surface-sensitive, and element-specific magnetometry method for insulating magnetic systems. Figure 2(b) displays the AHE results of a BiGa : TmIG(14.1μm)/Pt(10nm) Hall bar (Device 1) after the linear ordinary Hall effect background was subtracted. The first notable feature is that the residual hysteresis around zero field changes sign twice, first at around 135 K and second at around 60 K. As shown in Fig. 2(c), the 135 K AHE sign change accompanied with divergent coercivity is due to the compensation effect, consistent with VSM measurement [Fig. 1(e)]. The second sign change is possibly caused by the competition between SH-AHE and magnetic proximity effect-induced AHE (MP-AHE), the latter of which has an opposite sign compared with SH-AHE and is greatly enhanced at low temperatures [34]. The larger H_c estimated from the AHE loops as compared with that from the VSM measurement [Fig. 1(e)] is because VSM measures the overall magnetization of the millimeter-sized bulk sample, while AHE only probes the magnetization at the surface of ∼1 nm depth and in a local region of ∼100 μm width, which tends to behave more like a single domain and hence exhibits enhanced remanence and coercivity in hysteresis loops. Similar behavior was also observed in the MH loops of a TmIG film measured by VSM and MOKE techniques [6]. The second interesting feature of the AHE loops is that above T_{MC}, extra hysteresis appears in both positive and negative fields. As temperature approaches T_{MC} from 170 K, the center of the extra hysteresis moves from 3300 to 1100 Oe. The asymmetry between the left and right hysteresis is due to the slight temperature increase during the measurement. Similar anomalous hysteresis was also observed in RE-TM alloys [17,18,35]. There are two possible mechanisms for this behavior. The first is when there is chemical inhomogeneity, in certain temperature ranges the film is effectively composed of two exchange-coupled layers with different compensation temperatures [17,18]. The second possible reason for such triple hysteresis is first-order spin-flop phase transition where above a threshold field strength, the magnetizations of the two sublattices become noncollinear [35]. The spin-flop transition field required to counteract the strong exchange interaction is typically of the order of 10 T. Here, in the BiGa:TmIG films, the flipping fields are well below 1 T, which indicates that film inhomogeneity is the more likely reason for the observed anomalous hysteresis.

C. Internal exchange bias

XMCD [36,37] is based on the asymmetry between the resonant absorption of left and right circularly polarized x-rays by a magnetic material. Because each element has its characteristic electronic structure, XMCD has the advantage of being element-specific. Representative x-ray energy scans on the BiGa:TmIG film around the Fe L_3 and Tm M_5 edges are plotted in Fig. 3(a). At these edges, we obtained Fe and Tm sublattice hysteresis by scanning the external field, as shown in Figs. 3(b) and 3(c). Reversed XMCD signal is plotted as the y-axis so the sign in Fig. 3(b) directly reflects the polarity of Fe sublattice moment. The first important feature of the results is that at the extra hysteresis (e.g., 1200 Oe at 140 K), both Fe and Tm moments take a complete 180° flip, simultaneously. This safely rules out spin-flop phase transition as the reason

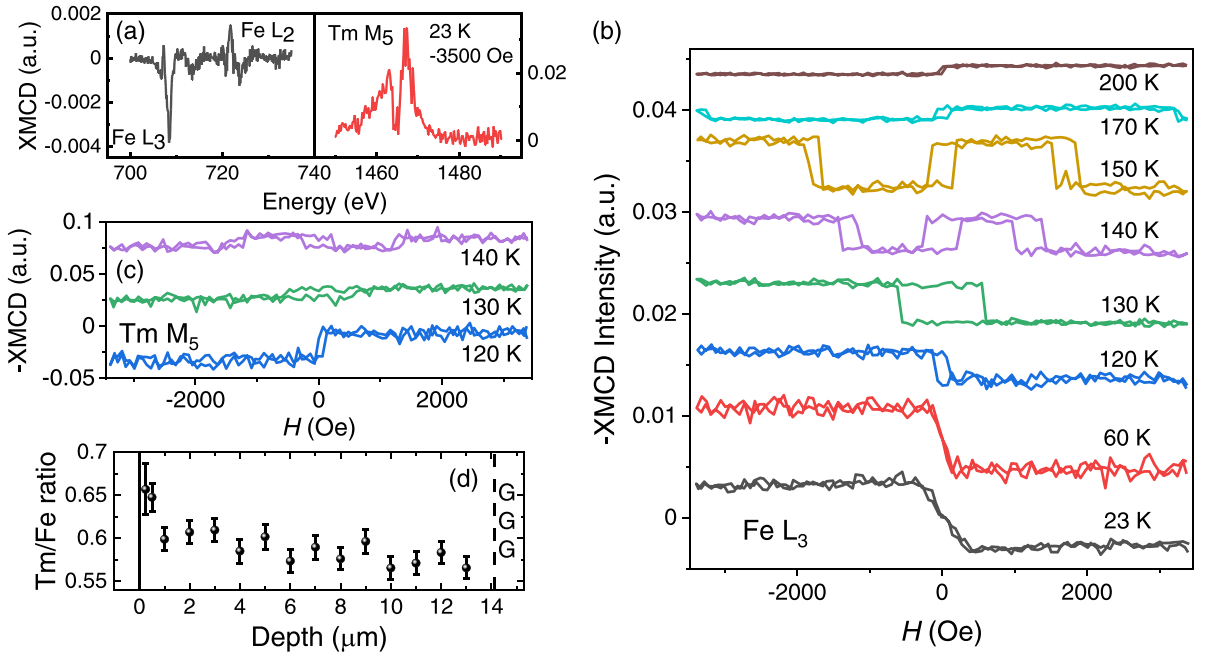

FIG. 3. (a) Representative XMCD energy scans at the Fe L_3 and Tm M_5 edges with a fixed external field. (b) and (c) Fe and Tm sublattice hysteresis were obtained by fixing energy at L_3 and M_5 peaks while scanning the external field applied normal to the sample surface. (d) Tm/Fe atomic ratio depth profile obtained by cross-sectional EDS measurement.

for the observed anomalous hysteresis and points its origin to be an EB effect possibly caused by film inhomogeneity. Besides, the sign change of the residual hysteresis from 140 to 130 K again shows 135 K as the MC point. Moreover, from 120 to 23 K, the Fe moment remains antiparallel to the external field [Fig. 3(b)], which confirms that the sign change of the AHE loop from 100 to 12 K [Fig. 2(b)] is indeed due to competing AHE mechanisms. By carrying out EDS measurements on a manually cut cross-section, we obtained Tm/Fe atomic ratio depth profile for the BiGa:TmIG film. Both the EDS sampling size and the depth are $\sim$1 μm. As can be seen in Fig. 3(d), the Tm/Fe ratio is much larger at the film surface (0.25 and 0.5 μm) than the rest of the bulk (1–13 μm). This indicates that the inhomogeneity is localized close to the sample surface, and it has a higher MC temperature compared with that of the bulk. Such different surface-bulk composition may be caused by the post-growth high-speed spinning process, but because of the continuous growth procedure, it is more likely that the Tm/Fe composition takes a continuous gradient instead of a sharp jump as in artificially engineered heterostructures. The existence of such composition gradient is supported by analyzing the temperature dependence of the EB field and the anisotropy energy, as shown in Appendix C.

The essence of the EB effect is the competition between the exchange and the Zeeman energies. As illustrated in Fig. 4, at 140 K, the BiGa:TmIG film can be divided into the Fe-dominant bulk part with a $T_{\mathrm{MC}}^{\mathrm{bulk}} \approx 135$ K and the Tm-dominant surface layer with a T_{MC} gradient ranging from about 140 to above 200 K [as shown in Sect. III D]. The thickness of the surface EB layer t_{EB} is defined as the distance from the sample surface to the MC boundary. In regime (i), the external field is smaller than the bias field H_{b}, defined as the center of the biased hysteresis, and exchange energy aligns

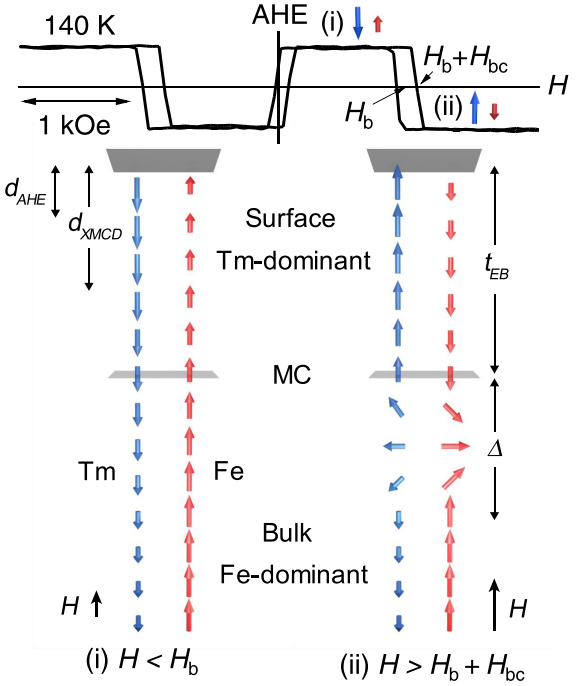

FIG. 4. (Top) AHE of Device A at 140 K as shown in Fig. 5. (Bottom) Illustration of the internal EB effect. Blue and red arrows represent the Tm and Fe magnetization, respectively. MC denotes the magnetization compensation boundary between surface and bulk. Only part of the bulk is drawn. In regime (i) $H < H_{\mathrm{b}}$, exchange energy aligns the surface moments with those of the bulk, while in regime (ii), an external field larger than $H_{\mathrm{b}} + H_{\mathrm{bc}}$ reverts the surface magnetization and a domain wall is formed beneath the MC boundary.

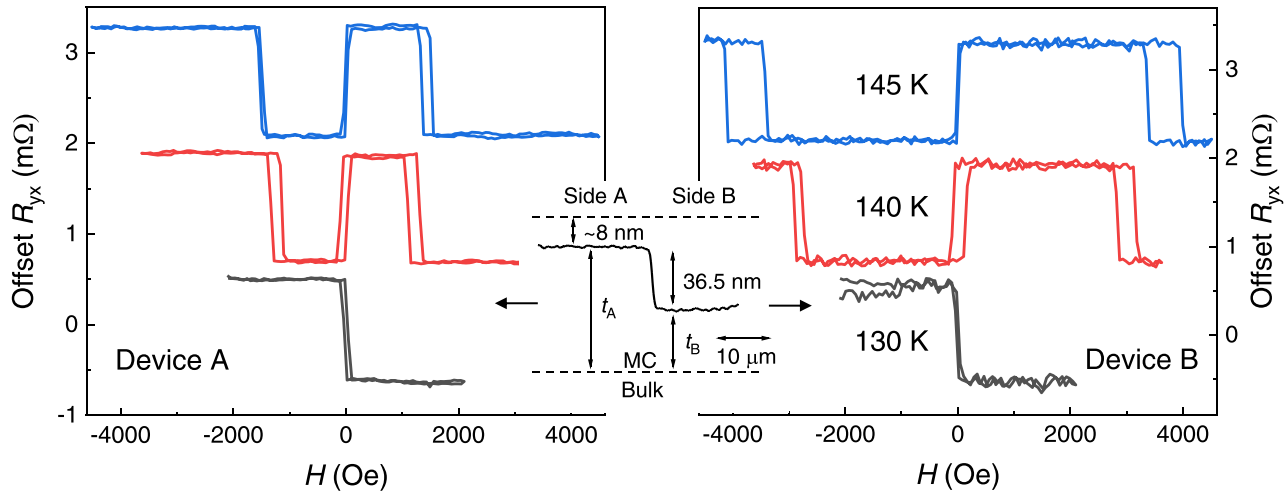

FIG. 5. AHE results of Hall bar Device A and B fabricated on Sides A and B, respectively, on a BiGa:TmIG film. Both devices share the same BiGa : TmIG(14.1 μm)/Pt(5 nm) structure and Hall bar geometry, and the measurements were done simultaneously. The inset is a cross-sectional AFM scan across the border between Sides A and B.

the Tm and Fe sublattices of the surface to those of the bulk, resulting in a positive AHE signal. However, because of being Tm-dominant, the net magnetization of the surface EB layer points opposite to the external field, which is unfavorable in terms of Zeeman energy. When the external field is increased above the threshold value $H_b + H_{bc}$, where H_{bc} is the coercivity of the biased hysteresis, it is more energy favorable for the surface to flip its magnetization while forming a domain wall at the MC boundary [regime (ii)]. The reversal of Fe sublattice moments at the surface gives a sign change in the AHE response. Here, we assume the 180° domain wall lies in the pinning bulk layer, just like the walls formed in the AF layer at the conventional AF/FM EB interfaces [11]. Since both AHE [Fig. 2(b)] and XMCD [Fig. 3(b)] measurements show a complete reversal of the biased hysteresis, this gives a lower bound of t_{EB} at 140 K as the XMCD probing depth $d_{XMCD} \sim 50$ nm. The domain-wall width Δ is estimated by the classical wall profile equation [38] $\Delta = \pi\sqrt{\frac{A}{K_u}} \approx 77$ nm, and the wall energy $\sigma_w = 4\sqrt{AK} \approx 0.24\,\mathrm{mJ/m^2}$. Here, the anisotropy energy $K_u = 2.49\,\mathrm{kJ/m^3}$ is extrapolated from IP VSM measurements (see Appendix A), and the exchange stiffness $A \sim 1.5\,\mathrm{pJ/m}$ is estimated by measuring the Curie temperature T_C and comparing with substituted garnets with a similar T_C and doping level (Appendix B).

By equaling the Zeeman and wall energies, we get the master equation of this internal EB effect [18]

$$H_b = \frac{\sigma_w}{2\mu_0 M_s^{avg} t_{EB}}, \tag{1}$$

where μ_0 is the vacuum permeability and M_s^{avg} is the average magnetization of the EB layer. With known H_b and σ_w, Eq. (1) can be utilized to estimate t_{EB}. As shown by the AFM scan in the inset of Fig. 5, we created a 36.5-nm step between Sides A and B on a BiGa:TmIG film by photoresist mask and ion-mill etching. The thicknesses t_A and t_B are defined as the distance between the MC boundary and the top of the surface. The ~8 nm difference between t_A and t_{EB} is from Piranha solution treatment used to recover the spin transmission of the sample surface from ion milling [24,25]. After fabrication of 5-nm Pt Hall bar devices with the same structure, we simultaneously carried out AHE measurements on Devices A and B, which are located on Sides A and B of the film, respectively. As can be seen in Fig. 5, the dramatic increase of H_b from 1200 (Device A) to 2900 Oe (Device B) at 140 K immediately suggests that t_A and t_B are comparable to the 36.5-nm step height. Besides, the enhanced AHE response in the acid-treated Devices A and B compared with Device 1 [Fig. 2(b)] made from the as-grown BiGa:TmIG film demonstrates that the spin transmission transparency at the BiGa:TmIG/Pt interface is greatly enhanced by the Piranha solution treatment, similar with the previous report on the yttrium iron garnet $Y_3Fe_5O_{12}$ (YIG)/Pt interface [24]. In order to account for the composition gradient in the EB layer, we simply assume a linear magnetization gradient,

$$M_s(t) = \frac{M_s^{surf}}{t_{EB}} t, \tag{2}$$

where M_s^{surf} is the saturation magnetization right at the original sample surface and t is the distance count from the MC boundary. Replacing $M_s^{surf} t_{EB}$ in Eq. (1) by $\int M_s(t)dt$ and taking H_b from AHE results on Devices A and B, we get $t_A \approx 67$ nm and the thickness of the original EB layer is $t_{EB} \approx 75$ nm at 140 K. Because the exact magnetization depth profile is unknown, this value only serves as an order of magnitude estimation and confirms that the inhomogeneity is indeed located very close to the sample surface, consistent with the EDS results [Fig. 3(d)].

D. The birth of a wall

Figure 6(a) displays the 200–250 K AHE loops of the same BiGa:TmIG/Pt Device 1 shown in Fig. 2(b). Although at 200 K, the EB layer still switches around $H_b = 7.6$ kOe in an abrupt and hysteretic way, similar to the results between 137 and 170 K [Fig. 2(b)], when temperature is increased to 230 or 250 K, a trend toward a gradual and reversible magnetization switching process is observed. Similar gradual reversal behavior of the EB layer is also observed through XMCD at the

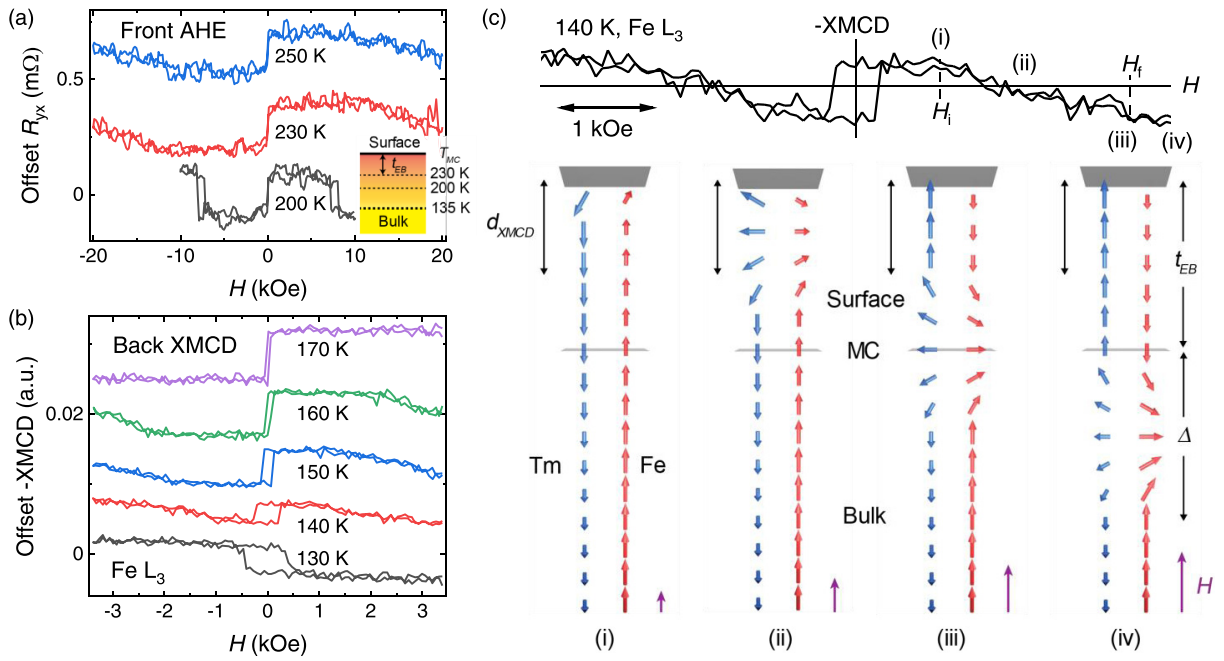

FIG. 6. (a) The 200–250 K AHE results of the same Device 1 shown in Fig. 2(b). (Inset) Schematic of the composition-gradient-caused T_{MC} gradient and the effective EB layer thickness. (b) Fe sublattice hysteresis measured by XMCD on the back side of the BiGa : TmIG(14.1 μm) sample. (c) (Top) Fe sublattice hysteresis at 140 K. (Bottom) Illustration of the proposed domain-wall motion model. At regime (i) $H = H_i$, the domain wall starts to enter the XMCD probing region which has a thickness of d_{XMCD}. In regime (ii) $H_i < H < H_f$, the partial domain wall is formed and probed by XMCD. At (iii) $H = H_f$, the wall leaves the XMCD probing region. And finally, when $H > H_f$ [regime (iv)], the wall is pushed below the MC boundary by the external field.

only measured spot on the film grown on the back side of the GGG substrate. As plotted in Fig. 6(b), the sign change of the residual hysteresis from 130 to 140 K proves the bulk of the backside film also has a MC temperature close to 135 K, same with the front side. However, above T_{MC}, the average magnetization in the XMCD-probed region changes in a gradual and nonhysteretic way. The reason for such crossover between different magnetization reversal mechanisms is still unclear. One possibility is associated with the thickness of the EB layer. As depicted in the inset of Fig. 6(a), as temperature rises, due to the composition as well as the compensation gradient close to the surface, the MC boundary between the bulk and the EB layer shifts up, and the effective t_{EB} becomes smaller. We speculate that when the EB layer thickness becomes very thin (compared with the domain-wall width), possibly due to the lack of domain-wall pinning sites, it will become more energy favorable for the EB layer to switch through a partial domain-wall formation process. As to the difference between the XMCD results on the front- and backside films [Figs. 3(b) and 6(b)], because of the inequivalent face-up and -down positions taken by the two sides during the post-growth spinning procedure, it is possible for the EB layers on the front and back sides to have different thicknesses and defect realizations. Despite the specific reason for this crossover as well as the exact wall profile being unknown, we can still draw a qualitative picture for the domain-wall formation process, as illustrated in Fig. 6(c). In regime (i), when an external field is applied and reaches H_i, the net magnetization in the most Tm-dominant surface layer starts to bend toward the field direction to lower the Zeeman energy. As the field increases, more and more Tm moments in the EB layer reorient toward a positive direction, causing the AF-coupled Fe moments to rotate toward negative direction, and a partial domain wall is formed in the XMCD-probed region with a thickness of d_{XMCD} [regime (ii)]. This shows up as a gradual decrease and sign change of the Fe sublattice XMCD intensity. In regime (iii), when $H = H_f$, the wall finishes its journey in the XMCD region, and the XMCD intensity is fully reversed. As the field further increases, the wall creeps down and finally arrives at its destination below the MC boundary [regime (iv)]. The reason for this field-driven domain-wall motion being gradual instead of abrupt may be a wall energy gradient in the vertical direction arising from a gradient in the anisotropy energy, exchange stiffness, or residual stress. Similar reversible behavior also exists in conventional magnetization reversal processes when the domain-wall motion is hindered by a potential energy [38].

IV. CONCLUSION

In conclusion, by utilizing transport and XMCD measurements, we probed the internal EB in a micrometer-thick BiGa:TmIG film due to composition inhomogeneities located close to the sample surface. By control experiments the thickness of the EB layer is calibrated to be at ∼100 nm order at 140 K. Possibly due to the change in the EB layer thickness as well as defect realization, a crossover from Stoner-Wohlfarth to domain-wall motion-type magnetization reversal process is observed. Our results show that the rich magnetization phase diagram of such compensated FI insulators can be probed by the low-cost, surface-sensitive, and element-specific AHE magnetometry method. When pushed down to the sub-100-nm thick limit by vapor-phase deposition

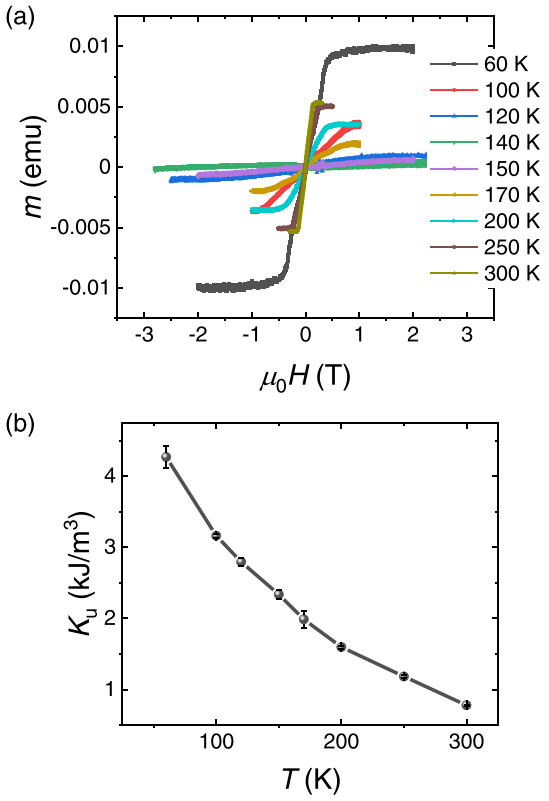

FIG. 7. (a) *MH* loops of a BiGa : TmIG(14.1 μm) sample with IP field scans. A linear paramagnetic background from GGG substrate is removed. (b) Calculated uniaxial anisotropy energy density as a function of temperature.

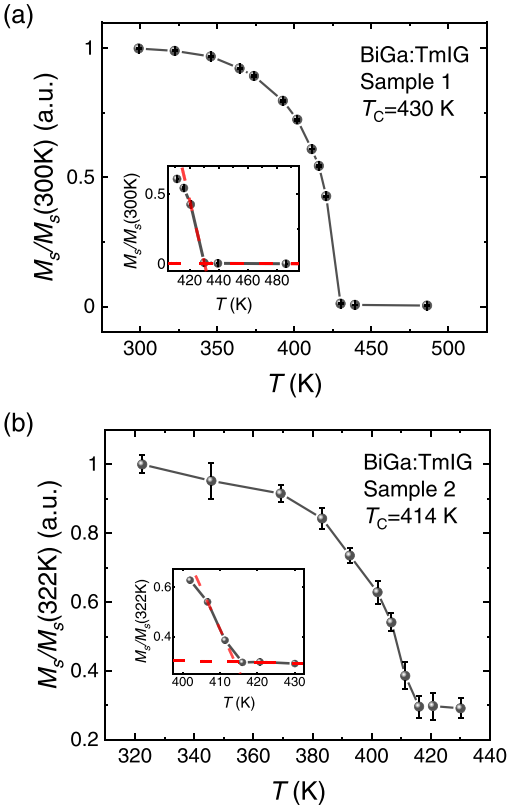

FIG. 8. (a) and (b) Saturation magnetization as a function of temperature for Sample 1 ($Bi_{0.63}Tm_{2.36}Ga_{1.15}Fe_{3.85}O_{12}$, 14.1 μm) and Sample 2 ($Bi_{0.5}Tm_{2.5}Ga_{1.3}Fe_{3.7}O_{12}$, 2 μm).

methods, these Bi- and Ga-doped TmIG films with tunable magnetization compensation, novel exchange bias effects, and enhanced magneto-optical responses may be promising for spintronic applications.

ACKNOWLEDGMENTS

We thank Y. Ji for use of the home-built transport measurement system and D. Li for assistance in XMCD measurements. Work at Bryn Mawr College is supported by the National Science Foundation (DMR #1708790). Use of the Advanced Photon Source is supported by the US Department of Energy, Office of Science, Office of Basic Energy Sciences under contract number DE-AC02-06CH11357. The work at Delaware was supported by the U.S. DOE, Office of Basic Energy Sciences, under contract number DE-SC0016380. The authors also acknowledge support from the University of Delaware for collaboration with Argonne National Laboratory.

APPENDIX A: MEASUREMENT OF THE UNIAXIAL ANISOTROPY ENERGY DENSITY

In order to estimate the uniaxial anisotropy energy density K_u, we carried out VSM measurement for a BiGa:TmIG(14.1 μm) sample with IP field scans, as plotted in Fig. 7(a). Then K_u is calculated with the equation $K_u = \frac{1}{2}\mu_0 M_s H_k$, where H_k is the anisotropy field obtained from the IP *MH* loops. As shown in Fig. 7(b), K_u gradually increases from 0.78 to 4.27 kJ/m$_3$ as the temperature decreases from 300 to 60 K. Because of the large H_k at 140 K exceeds our instrument field limit (3 T), K_u at this temperature is extrapolated from the $K_u - T$ curve as 2.49 $\pm$ 0.06 kJ/m$_3$, where the uncertainty is taken as the average from the measured K_u points.

APPENDIX B: ESTIMATION OF THE EXCHANGE STIFFNESS FROM T_C

Pure YIG has a Curie temperature of 560 K [39] and an exchange stiffness of 4.15 pJ/m [40]. In Ga^{3+} or Ge^{3+} substituted iron garnets, because of the reduction in Fe^{3+}-O^{2-}-Fe^{3+} superexchange interaction, both the Curie temperature T_C and the exchange stiffness A are reduced. In order to estimate the exchange stiffness of our BiGa:TmIG films, we measured *MH* loops for Sample 1 and Sample 2 between 300 and 500 K in the VSM oven mode, and the obtained M_s vs T curves are shown in Fig. 8. Because the sample and the thermocouple are on opposite sides of the sample holder, the real sample temperature was calibrated by measuring the M_s vs T curve of a La-doped YIG crystal with a known Curie temperature (560 K). From Fig. 8, the Curie temperature for Sample 1 and Sample 2 is extrapolated to be 430 and 414 K, respectively. By comparing with the Ga^{3+} or Ge^{3+} substituted garnets with a similar T_C and composition [41,42], the exchange stiffness of Sample 1 and 2 is estimated to be ~1.5 and 1.2 pJ/m, respectively.

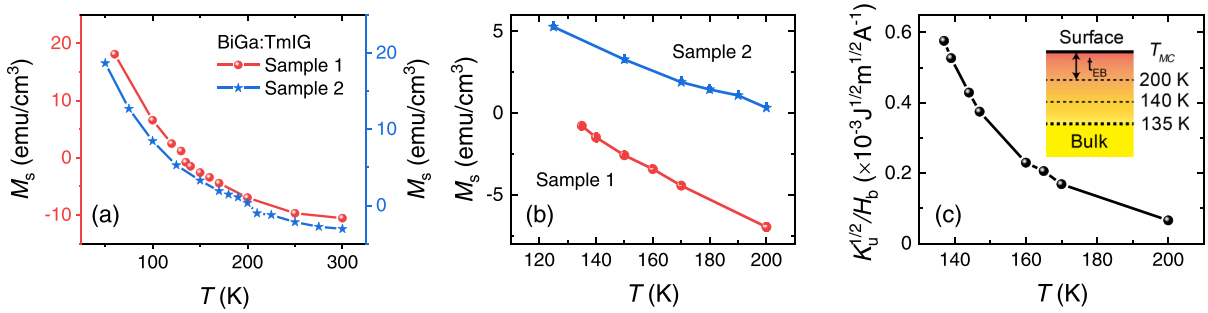

FIG. 9. (a) Saturation magnetization as a function of temperature for Sample 1 and Sample 2. A positive M_s value means Tm dominant and negative Fe dominant. (b) M_s vs T between 135 and 200 K. (c) $\sqrt{K_u}/H_b$ as a function of temperature. The inset is an illustration of the composition gradient in the EB layer.

APPENDIX C: TRANSPORT EVIDENCE FOR THE COMPOSITION GRADIENT IN THE EB LAYER

As shown in Fig. 9(a), despite the different composition and absolute M_s values, the sign-included M_s for Samples 1 and 2 has a similar temperature dependence. Moreover, between 135 and 200 K, it has an approximate linear relationship with T [Fig. 9(b)], which can be written as

$$M_s = aT + b, \tag{C1}$$

where a and b are linearization constants between 135 and 200 K. From the EB Eq. (1) and the wall energy expression $\sigma_w = 4\sqrt{AK_u}$, we can get the following relation,

$$\frac{\sqrt{K_u}}{H_b} = \frac{\mu_0 M_s t_{EB}}{2\sqrt{A}} = \frac{\mu_0 a t_{EB}}{2\sqrt{A}}T + \frac{\mu_0 b t_{EB}}{2\sqrt{A}}. \tag{C2}$$

Since A only slightly decreases in the measured temperature range [42,43], if the EB layer is a single uniform layer, one should expect an almost linear relation between $\frac{\sqrt{K_u}}{H_b}$ and T, just like M_s vs T [Fig. 9(b)]. However, when the measured $\frac{\sqrt{K_u}}{H_b}$ is plotted as a function of temperature [Fig. 9(c)], a clear deviation from linear dependence is observed. When T increases from 137 to 200 K, the slope of the $\frac{\sqrt{K_u}}{H_b}$ vs T curve decreases by an order of magnitude. This can only be explained by a reduced effective t_{EB} as temperature increases. Thus, Fig. 9(c) serves as evidence for a composition gradient in the EB layer, in which when moving from the bulk to the surface, both the Tm/Fe ratio and the MC temperature T_{MC} gradually increase, as depicted in the inset of Fig. 9(c).

[1] J. Finley and L. Liu, Appl. Phys. Lett. **116**, 110501 (2020).
[2] J. Finley and L. Liu, Phys. Rev. Appl. **6**, 054001 (2016).
[3] S. A. Siddiqui, J. Han, J. T. Finley, C. A. Ross, and L. Liu, Phys. Rev. Lett. **121**, 057701 (2018).
[4] K. Cai, Z. Zhu, J. M. Lee, R. Mishra, L. Ren, S. D. Pollard, P. He, G. Liang, K. L. Teo, and H. Yang, Nat. Electron. **3**, 37 (2020).
[5] M. Kubota, A. Tsukazaki, F. Kagawa, K. Shibuya, Y. Tokunaga, M. Kawasaki, and Y. Tokura, Appl. Phys. Express **5**, 103002 (2012).
[6] C. O. Avci, A. Quindeau, C.-F. Pai, M. Mann, L. Caretta, A. S. Tang, M. C. Onbasli, C. A. Ross, and G. S. D. Beach, Nat. Mater. **16**, 309 (2016).
[7] Q. Shao, Y. Liu, G. Yu, S. K. Kim, X. Che, C. Tang, Q. L. He, Y. Tserkovnyak, J. Shi, and K. L. Wang, Nat. Electron. **2**, 182 (2019).
[8] A. Quindeau, C. O. Avci, W. Liu, C. Sun, M. Mann, A. S. Tang, M. C. Onbasli, D. Bono, P. M. Voyles, Y. Xu, J. Robinson, G. S. D. Beach, and C. A. Ross, Adv. Electron. Mater. **3**, 1600376 (2016).
[9] P. Hansen and W. Tolksdorf, J. Appl. Phys. **369**, 4577 (1991).
[10] W. H. Meiklejohn and C. P. Bean, Phys. Rev. **102**, 1413 (1956).
[11] F. Radu and H. Zabel, Springer Tracts Mod. Phys. **227**, 97 (2008).
[12] P. J. van der Zaag, R. M. Wolf, A. R. Ball, C. Bordel, L. F. Feiner, and R. M. Jungblut, J. Magn. Magn. Mater. **148**, 346 (1995).
[13] F. Hellman, R. B. van Dover, and E. M. Gyorgy, Appl. Phys. Lett. **50**, 296 (1987).
[14] F. Canet, S. Mangin, C. Bellouard, and M. Piecuch, Europhys. Lett **52**, 594 (2000).
[15] C. Schubert, B. Hebler, H. Schletter, A. Liebig, M. Daniel, R. Abrudan, F. Radu, and M. Albrecht, Phys. Rev. B **87**, 054415 (2013).
[16] F. Radu, R. Abrudan, I. Radu, D. Schmitz, and H. Zabel, Nat. Commun. **3**, 715 (2012).
[17] S. Esho, Jpn. J. Appl. Phys. **15**, 93 (1976).
[18] O. S. Lutes, J. O. Holmen, R. I. Kooyer, and O. S. Aadland, IEEE Trans. Magn. **13**, 1615 (1977).
[19] K. Chen, D. Lott, F. Radu, F. Choueikani, E. Otero, and P. Ohresser, Sci. Rep. **5**, 18377 (2015).
[20] C. Luo, H. Ryll, C. H. Back, and F. Radu, Jpn. Sci. Rep. **9**, 18169 (2019).
[21] I. I. Syvorotka, I. M. Syvorotka, S. B. Ubizskii, P. Kumar, and A. Prabhakar, *International Conference on Oxide Materials for Electronic Engineering - fabrication, properties and applications* (Lviv, Ukraine, OMEE-2014), pp. 201-202.
[22] D. Zhang, B. Mei, H. Zhang, Q. Yang, and Y. Rao, IEEE Trans. Magn. **51**, 11 (2015).

[23] S. S. Dash, P. Mukherjee, D. Haskel, R. A. Rosenberg, and M. Levy, Optica **7**, 1038 (2020).
[24] M. Li, L. Jin, Z. Zhong, X. Tang, Q. Yang, L. Zhang, and H. Zhang, Phys. Rev. B **102**, 174435 (2020).
[25] M. Li, D. Zhang, L. Jin, B. Liu, Z. Zhang, X. Tang, H. Meng, Q. Yang, L. Zhang, and H. Zhang, Appl. Phys. Lett. **118**, 042406 (2021).
[26] K. Momma and F. Izumi, J. Appl. Crystallogr. **44**, 1272 (2011).
[27] S. Geller, J. Appl. Phys. **31**, S30 (1960).
[28] T. B. Mitchell and P. E. Wigen, J. Appl. Phys. **61**, 3259 (1987).
[29] P. Hansen and K. Witter, J. Appl. Phys. **58**, 454 (1985).
[30] J. Sinova, S. O. Valenzuela, J. Wunderlich, C. H. Back, and T. Jungwirth, Rev. Mod. Phys. **87**, 1213 (2015).
[31] Y.-T. Chen, S. Takahashi, H. Nakayama, M. Althammer, S. T. B. Goennenwein, E. Saitoh, and G. E. W. Bauer, Phys. Rev. B **87**, 144411 (2013).
[32] Y. Lim, B. Khodadadi, J.-F. Li, D. Viehland, A. Manchon, and S. Emori, Phys. Rev. B **103**, 024443 (2021).
[33] A. Ghosh, S. Auffret, U. Ebels, and W. E. Bailey, Phys. Rev. Lett. **109**, 127202 (2012).
[34] Q. Shao, A. Grutter, Y. Liu, G. Yu, C. Y. Yang, D. A. Gilbert, E. Arenholz, P. Shafer, X. Che, C. Tang, M. Aldosary, A. Navabi, Q. L. He, B. J. Kirby, J. Shi, and K. L. Wang, Phys. Rev. B **99**, 104401 (2019).
[35] A. Pogrebna, K. Prabhakara, M. Davydova, J. Becker, A. Tsukamoto, T. Rasing, A. Kirilyuk, A. K. Zvezdin, P. C. M. Christianen, and A. V. Kimel, Phys. Rev. B **100**, 174427 (2019).
[36] J. Stöhr and H. C. Siegmann, *Magnetism: From Fundamentals to Nanoscale Dynamics* (Springer-Verlag, Berlin, 2006).
[37] G. van der Laan and A. I. Figueroa, Coord. Chem. Rev. **277-278**, 95 (2014).
[38] B. D. Cullity and C. D. Graham, *Introduction to Magnetic Materials* (Wiley, Hoboken, NJ, 2009).
[39] V. Cherepanov, I. Kolokolov, and V. Lvov, Phys. Rep. **229**, 81 (1993).
[40] R. D. Henry and D. M. Heinz, AIP Conf. Proc. **18**, 194 (1974).
[41] A. C. Gerhardstein, P. E. Wigen, and S. L. Blank, Phys. Rev. B **18**, 2218 (1978).
[42] R. C. LeCraw and L. R. Walker, J. Appl. Phys. **32**, 167S (1961).
[43] J. T. Carlo, D. C. Bullock, and F. G. West, IEEE Trans. Magn. **10**, 626 (1974).